Highlights

- TTM–MD model reveals a novel interfacial stripping mechanism in layered materials.
- Short laser pulse durations facilitate interfacial stripping.
- Atomistic insights reveal ultrafast lasers save energy and improve quality.
- Femtosecond lasers enable high-quality, low-damage removal of Al on GFRP.
- Multitechnique characterization confirms nanoscale thermal oxidation and damage.

Journal Pre-proof

Huang, Z., Feng, Z., Cai, Y., Zhang, T., Tang, Y., Li, X., Liang, X., Luo, X., & Liu, Z. (2025). Atomistic insights of thermomechanical interfacial stripping—a pathway to low-damage femtosecond laser processing of layered materials. Journal of Materials Science and Technology. https://doi.org/10.1016/j.jmst.2025.12.035. For the purpose of open access, a CC BY 4.0 licence has been applied.

Research Article

Atomistic insights of thermomechanical interfacial stripping—a pathway to low-damage femtosecond laser processing of layered materials

Zhidong Huang [a, b, c], Zeming Feng [a, b, c], Yukui Cai [a, b, c, d, *], Teng Zhang [e], Yunqing Tang [a, b, c, d], Xing Li [a, b, c, d], Xiaoliang Liang [a, b, c, d], Xichun Luo [f], Zhanqiang Liu [a, b, c, d]

[a] School of Mechanical Engineering, Shandong University, Jinan 250061, China

[b] Shandong Key Laboratory of High Performance Tools and System, Jinan 250061, China

[c] Key Laboratory of High Efficiency and Clean Mechanical Manufacture of Ministry of Education, Jinan 250061, China

[d] State Key Laboratory of Advanced Equipment and Technology for Metal Forming, Shandong University, Jinan 250061, China

[e] AVIC Research Institute for Special Structures of Aeronautical Composite, Aviation Key Lab of Science and Technology on High Performance Electromagnetic Windows, Jinan 250023, China

[f] Centre for Precision Manufacturing, DMEM, University of Strathclyde, G1 1XJ Glasgow, United Kingdom

[*] Corresponding author.

E-mail address: caiyukui@sdu.edu.cn (Y.K. Cai).

Keywords: Femtosecond laser ablation; Two-temperature model-molecular dynamic simulation; Layered materials; Laser selective removal

Journal Pre-proof

Abstract

The micropatterning of multilayer composites enables advanced performance and tailored electromagnetic functionalities. However, precisely removing surface coatings while minimizing substrate damage remains a critical manufacturing challenge. Although femtosecond (fs) lasers are well-established for high-precision ablation with minimal thermal damage, their interactions with layered material interfaces are still poorly understood. Here, we investigate the mechanisms and process of the fs laser ablation of an aluminum film on a glass-fiber-reinforced polymer substrate. Using an extended two-temperature model-molecular dynamics framework for multilayer materials and in situ high-speed imaging of fs laser processing dynamics, we identify and validate a unique thermomechanical removal mechanism: interfacial stripping. Ultrashort laser pulses induce high compressive stresses that propagate into the material and reflect as tensile waves, exceeding the metal's yield strength and causing spallation. The substrate is compressed near its elastic limit and rebounds, propelling the residual metal layer forward. Interfacial stripping occurs when the translational kinetic energy surpasses the interfacial bonding energy. Atomistic insights reveal that interfacial stripping minimizes the heat-affected zone, enables thickness-adaptive removal, and avoids vaporization, thereby achieving low damage, low energy consumption, and superior quality. Experimentally, we achieve complete metal removal with optimized laser parameters. Multi-method characterizations elucidate the thermochemical damage mechanisms of the epoxy substrate, confirming that damage is confined to the nanoscale. Combining atomic-scale simulation, in situ imaging, and multi-technique ex situ characterization, this work demonstrates the unique advantages of the ultrafast laser processing of layered materials.

1. Introduction

Journal Pre-proof

Multilayer composites are progressively replacing traditional homogeneous materials to address the growing demand for lightweight and multifunctional integration in aerospace [1–3], microelectronics [4,5], and communication applications [6]. In these fields, various functional elements, including conductive circuits [7,8], frequency-selective surfaces for radomes [9], and sensing systems [4,10,11], are typically fabricated by selectively removing the surface coating in such complex structures. However, achieving this requires complete coating removal while minimizing substrate damage, which remains a significant manufacturing challenge [6,12,13].

Ultrafast pulsed lasers, characterized by ultrashort durations and high peak intensities, enable noncontact processing with exceptional precision [14,15]. Such ultrashort pulses suppress thermal diffusion, minimizing substrate damage while achieving submicron removal precision. Integrated with high-speed scanning galvanometers, ultrafast lasers exhibit superior processing quality across diverse layered material systems, including carbon films on polymer substrates [12], metallic films on resin/glass/ceramic substrates [5,6,16,17], and functional electrode materials [18,19], as well as in laser cleaning applications [20]. Furthermore, in situ sensing technologies have been incorporated for online monitoring and process control [5,21,22].

Despite significant progress in laser processing techniques and equipment for layered materials, the fundamental mechanisms governing material removal at heterogeneous interfaces remain inadequately elucidated. The two-temperature model (TTM) has been widely used to describe the nonequilibrium thermal response in ultrafast laser-matter interactions [23,24]. For layered systems, He et al. [2] identified thermal ablation and mechanical stripping as two distinct material removal mechanisms under nanosecond (ns) pulse irradiation, with their simulations highlighting the significance of interfacial thermal stress. Complementing continuum models, molecular dynamics (MD) simulations offer atomic-scale insights into

phase transitions and ablation dynamics. To bridge these scales, the integrated TTM-MD framework [25–27] thus enabled a comprehensive atomistic investigation, validated across multiple material categories, including metallic systems (e.g., Al [28], Ni [29,30], Cu [31–33], and Au [34–37]), alloys [38–40], semiconductors [41,42], and diamond [43]. This approach established vaporization, spallation, and phase explosion as the dominant ablation mechanisms [25,26,30,44]. Notably, studies on bilayer metals (Au/Ti and Ni/Al) revealed that interfacial pressure resulting from thermodynamic mismatch could drive a thermomechanical removal process [45,46]. However, removal mechanisms at interfaces involving nonmetallic substrates like polymers are still poorly understood, necessitating further research into thermodynamic incompatibility and stress propagation.

Given the critical role of glass-fiber-reinforced polymer (GFRP) substrates in electronics and aerospace [5,47], this study investigates the mechanisms and processes involved in the femtosecond (fs) laser removal of metallic films from GFRP substrates. Combining TTM-MD simulations with in situ high-speed imaging, we unveil and validate a unique interfacial stripping mechanism. These atomistic insights provide explanations for the origins of fs laser manufacturing advantages, including high precision, minimal damage, and low energy consumption. Experimentally, we demonstrate complete ablation of the aluminum layer and show that the resulting thermal damage to the underlying substrate is confined to the nanoscale, as confirmed by comprehensive morphological, chemical, and mechanical characterization.

2. Experiments and computations

2.1. Laser processing and characterization

As depicted in Fig. 1(a), the sample consisted of aluminum-coated GFRP with a total thickness of ~1 mm, comprising a surface Al layer, an epoxy adhesive, and a reinforced glass fiber layer. The GFRP composite was formed by impregnating a woven glass fiber cloth with

epoxy resin binder. A 4 μm-thick aluminum film (Fig. S1 in the Supplementary Materials) was thermally pressed onto the epoxy surface to form a stable interfacial connection.

An infrared fs laser (YSLP Ltd, wavelength: 1030 nm; maximum output power: 40 W; pulse duration: 350 fs) was used to remove the Al film from the epoxy substrate. A galvanometer scanner focused the Gaussian beam to a spot of ~20 μm on the sample surface.

A high-speed camera (Phantom V2012), coupled with an objective lens (35 ×), captured the kinetic behavior during fs laser processing. To facilitate observation of the cross-section, a thicker metal film (~73 μm) was ablated via continuous line scanning perpendicular to the material edge. The recording speed was set to ~67000 frames per second, corresponding to approximately one frame every two laser pulses at a repetition rate of 100 kHz. To prevent image distortion from overexposure to the fs laser, an optical filter with a pass-through wavelength of 640 nm blocked the fs laser light, while an illumination laser of the same wavelength provided precise imaging. ImageJ software was used for image binarization and tracking of the ejected molten droplets [48].

Confocal laser scanning microscopy (CLSM, Keyence) was employed to characterize surface morphology, roughness (Ra), and ablation depth. A scanning electron microscope (SEM, JSM-7610) combined with energy-dispersive X-ray spectroscopy (EDS, Oxford Instruments) was used for elemental mapping to assess substrate damage and residual metal film. X-ray photoelectron spectroscopy (XPS, Thermo Fisher) and Fourier transform infrared spectroscopy (FTIR, Horiba) were employed to evaluate the thermal and oxidative degradation of the resin matrix. A nanoindenter (Bruker) and a Vickers microhardness tester (Wilson) were employed to probe the mechanical properties of the substrate surface at different depth scales.

Journal Pre-proof

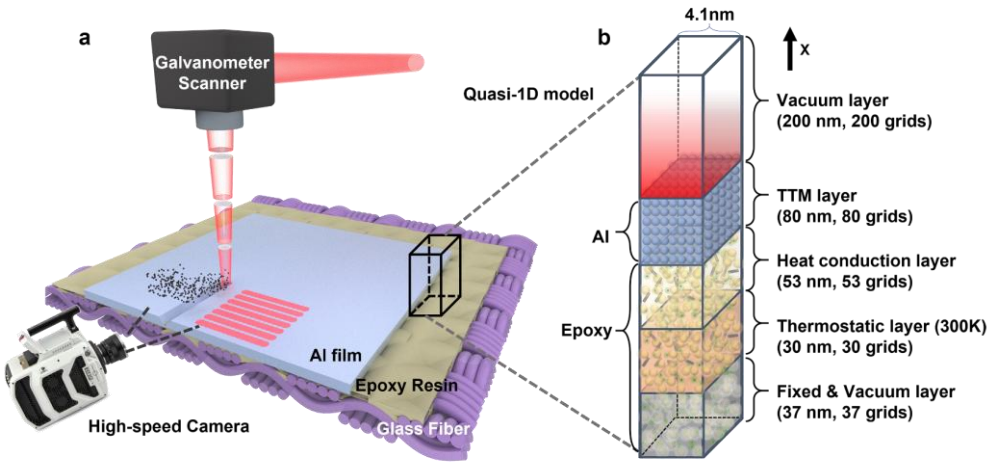

Fig. 1. (a) Schematic diagram of the experimental setup and materials. (b) Details of the quasi-1D TTM-MD model.

2.2. Computational methodology

The TTM-MD method was employed to simulate the fs laser ablation process. This method combined the TTM model, which described ultrafast laser-induced nonequilibrium heat transfer between the electron and lattice subsystems [49], with MD for tracking atomic-scale phase transitions and ablation dynamics [31]. The two models were coupled by calculating the electron temperature at the continuum scale and overlapping it with the MD lattice grid [27,29,50,51]. The entire framework was performed using LAMMPS [52].

The hybrid system, shown in Fig. 1(b), comprised an epoxy resin substrate and an 80-nm-thick aluminum film. The epoxy substrate was constructed and cross-linked using Materials Studio and described by the consistent valence force field in LAMMPS [53]. The aluminum film was modeled using the embedded atom method potential [54]. The interfacial adhesion between the metal and the substrate was governed by nonbonded van der Waals and Coulombic interactions [55].

The total model thickness was 400 nm, divided into five regions along the *x*-axis: a 200-nm vacuum layer for accommodating ablated material, the TTM-active region, a heat conduction layer, as well as a thermostatic layer and a fixed atomic layer, which together

constituted a non-reflecting boundary [56,57]. The detailed thermodynamic parameters for aluminum, model construction procedures, and interaction potentials were provided in the Supplementary Materials.

3. Results and discussion

3.1. TTM-MD simulation

3.1.1. fs laser ablation of the metal film

Previous TTM-MD studies have predominantly focused on ultrafast laser ablation of pure metals, revealing vaporization, spallation, and phase explosion as dominant removal mechanisms [25,29–31,39,58,59]. Using the same methodology, we simulated fs laser ablation of an Al film on an epoxy substrate. The observed mechanisms aligned with previous findings. Fig. 2(a) shows atomic trajectories at a pulse duration of 350 fs and an absorbed energy density (fluence) of 0.22 J/cm^2. Only the critical region near the metal-epoxy interface is displayed, with interfacial atoms marked in black. The center symmetry parameter (CSP) [60] is used to distinguish phase states and transitions in metallic crystals. Generally, values below 6 indicate a solid state (blue), values between 6 and 12 correspond to a liquid state (green to yellow), and values above 12 indicate a gaseous state (red) [59]. Fig. 2(b and c) shows the spatiotemporal evolution of lattice temperature and pressure, respectively. The x-axis represents time, while y = 0 corresponds to the surface where the metal is in contact with the vacuum. The positive y denotes the vacuum region, and the negative direction represents the material bulk. The compressive pressure is marked in red, whereas the tensile pressure is shown in blue.

Journal Pre-proof

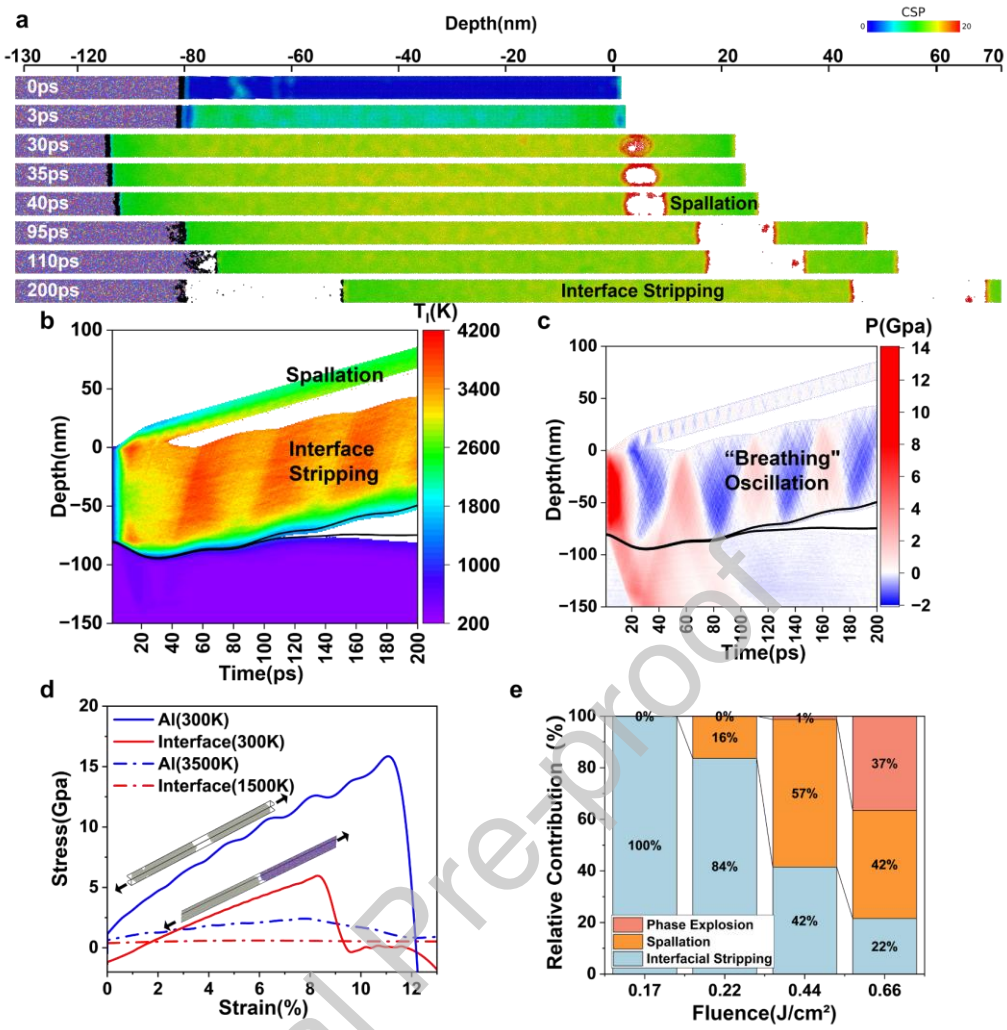

Fig. 2. TTM-MD simulation results of fs laser irradiation on an 80 nm-thick Al film with a 350 fs pulse and 0.22 J/cm^2 fluence. (a) Atomic snapshots (Movie S1). (b and c) Spatiotemporal distributions of (b) lattice temperature and (c) pressure. (d) Quasistatic tensile stress-strain curves for pure Al and the Al/epoxy interface obtained from MD simulations. (e) Fluence-dependent contribution of the three mechanisms, quantified by statistically analyzing the number of atoms removed via each mechanism.

Metal removal is initiated by spallation. At 0 ps, the solid aluminum film exhibits a perfectly ordered face-centered cubic crystal structure with a CSP of 0. Driven by rapid electronic thermal conduction and electron-lattice coupling, most of the metal melts within ~3 ps. As shown in Fig. 2(b and c), the temperature surges to ~1500 K, exceeding the melting point (933 K), and induces intense compressive stresses up to 14 GPa. Concurrently, thermal

expansion increases the film thickness from 80 to 117 nm at 30 ps, as recorded in Fig. 2(a). The resulting compressive stress wave propagated through the film thickness and reflected upon reaching the free surfaces (vacuum and epoxy interface). According to stress wave propagation theory, such reflection at a free surface caused phase inversion, generating a tensile (rarefaction) wave back into the material. This tensile stress stretched the metal and nucleated voids near the vacuum surface. These voids grew and culminated in complete rupture by 40 ps, ejecting a 21-nm-thick surface layer at 450 m/s.

Laser-induced spallation is a distinctive material removal mechanism in ultrafast laser ablation of metals [29–31,39]. It arises from the significant temporal mismatch between the ultrashort laser pulse duration and the mechanical relaxation time of the material. The mismatch confines deposited energy, generating substantial compressive stresses. Upon reflection at free surfaces, the resultant tensile stress can surpass the transient yield strength of the metal, breaching the stress confinement and triggering material ejection as large clusters and small droplets [30,44]. As corroborated by thermal activation theory [61] and MD simulations [62], the yield strength of metals decreases markedly with increasing temperature. For Al, the yield strength diminished to ~2.4 GPa at a high temperature of 3500 K, based on the data in Fig. 2(d). As shown in Fig. 2(b and c), the metal temperature in our simulation exceeds 3500 K at 30 ps, while the laser-induced tensile stress reaches a comparable magnitude of ~2 GPa. The minor difference of ~0.4 GPa could be attributed to the more violent metal motion during the spallation process, causing slightly earlier fracture compared to the quasistatic tensile test. This combination of sufficient tensile stress and reduced yield strength fulfills the critical conditions for spallation.

In Fig. 2(c), following spallation at 40 ps, the residual metal film exhibits periodic stress oscillations, with alternating tensile and compressive phases of gradually diminishing peak amplitudes. Because the resin had a lower acoustic impedance than the metal, the stress waves

Journal Pre-proof

reaching the Al/epoxy interface were reflected as inverted waves, analogous to those at a free surface. Successive reflections between the two interfaces led to sustained tensile-compressive cycling, manifesting as a characteristic "breathing" oscillation. Energy dissipation through frictional mechanisms gradually attenuated the intensity of the stress waves.

3.1.2. Interfacial stripping removal mechanism

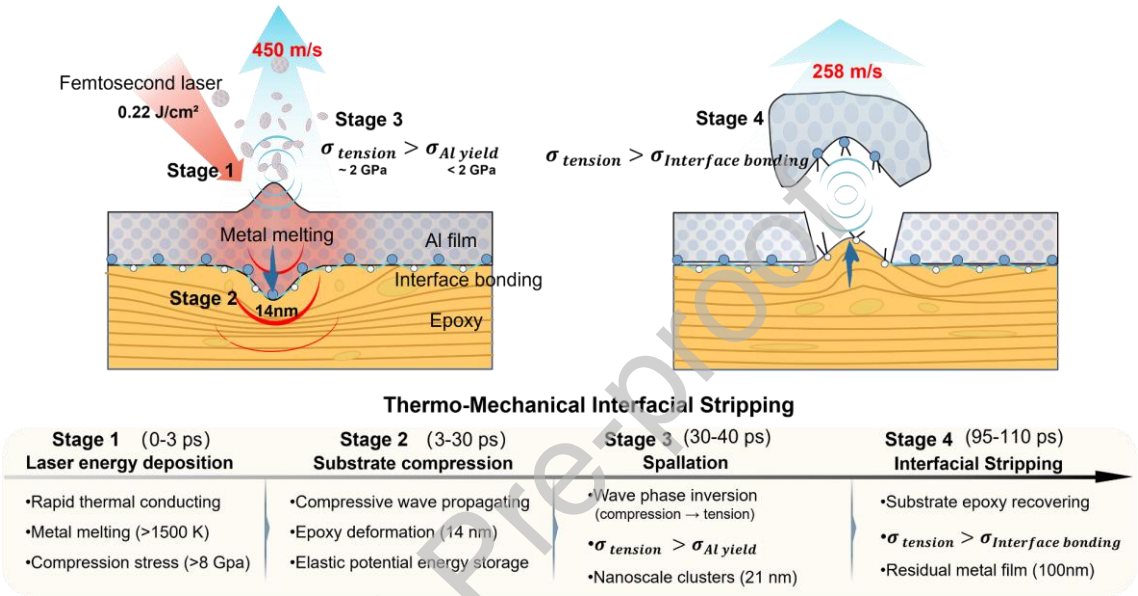

Fig. 3. Schematic of the interfacial stripping removal mechanism.

Beyond spallation, we identified interfacial stripping as another thermomechanical removal mechanism specific to layered materials. Driven by the thermal expansion of the metal layer, substantial compressive stress was transmitted to the epoxy substrate, compressing it by up to 14 nm at 30 ps. The epoxy then rebounded, fully recovering its thickness by 95 ps and propelling the overlying metal forward. Driven by inertia, the residual metal film continued to move forward. Meanwhile, the epoxy, which was fixed at its base and constrained by interfacial bonding, underwent tensile deformation and gradually decelerated. The metal and epoxy at the interface initially maintained the same speed. However, as the epoxy continued to stretch, the tensile force increased and eventually exceeded the interfacial bonding strength. Consequently, the interfacial bond failed, ejecting the metal layer at 258 m/s at 110 ps. The epoxy then contracted and returned to its original thickness by 200 ps. Fig. 3 illustrates the complete

process, encompassing both spallation and interfacial stripping. From an energy perspective, the epoxy substrate behaved like a spring. The compressive stress stored elastic potential energy, which was converted into translational kinetic energy (different from thermal vibrational kinetic energy) during rebound. Interfacial stripping initiated once the metal's kinetic energy surpassed the interfacial bonding energy.

Interfacial stripping and metal spallation are both driven by ultrafast laser-induced stress waves but differ in their failure location and triggering conditions. Spallation requires tensile stress exceeding the metal's transient strength, whereas interfacial stripping occurs when stress surpasses the interfacial bond strength. Quasistatic tensile simulations were performed on isolated Al metal and Al/epoxy interface models at 300 K and elevated temperatures, as presented in Fig. 2(d). At 300 K, the interfacial yield strength is calculated to be ~6 GPa, much lower than the yield strength of aluminum (~17 GPa), indicating a roughly threefold difference. Under in situ high-temperature conditions, the yield strength of aluminum decreases to ~2.4 GPa at 3500 K, while that near the interface approaches zero at 1500 K. These results further show that the combination of laser-induced high pressure and thermally driven interfacial adhesion failure is the key mechanism responsible for mechanical removal. This significant disparity explains why interface-driven stripping dominates in Al/epoxy systems. By adjusting the laser fluence and film thickness (Figs. S2 and S3), pure interfacial stripping was even achieved without concurrent metal spallation.

Under the same total ablation volume condition, the laser fluence level significantly influences the competition among different ablation mechanisms. At a near-threshold fluence of 0.17 J/cm^2, only interfacial stripping occurs (Fig. S3). When the fluence increases to 0.22 J/cm^2, a single spallation event takes place and ceases after 40 ps (Fig. 2). Further increasing the fluence to 0.44 J/cm^2 induces continuous spallation up to five times within a single laser pulse (Fig. S4). At 0.66 J/cm^2, in addition to spallation, the material disintegrates into smaller

metal clusters that are ejected at higher velocities—a characteristic phenomenon of phase explosion (Fig. S5). These observations demonstrate that the dominant removal mechanism is governed by the incident laser energy. As shown in Fig. 2(e), cluster analysis was used to quantify the proportion of atoms removed by each mechanism. With increasing fluence, the relative contributions of spallation and phase explosion gradually rise, while that of interfacial stripping diminishes. Therefore, applying a fluence close to the interfacial stripping threshold allows optimal outcomes with minimal energy input, thus achieving maximum process efficiency.

3.1.3. Long-pulse laser ablation

To investigate the influence of laser pulse duration, MD simulations were performed for a 1-ns laser pulse. The interaction between long-pulse lasers and materials was dominated by heat conduction, and energy transfer between electrons and lattices could be neglected [25]. Therefore, a depth-dependent heat source, following the Beer-Lambert law [63–65], was applied directly to the metal at a fluence of 27.5 J/cm^2. Although this value was 125 times higher than that of the fs pulse, the corresponding power density was only 4.3%. Consistently, Fig. 4(a) shows the atomic trajectories, while Fig. 4(b and c) shows the spatiotemporal evolution of lattice temperature and pressure, respectively. Furthermore, Fig. 4(d) shows the metal phase transition throughout ablation, as classified by the CSP criterion.

Journal Pre-proof

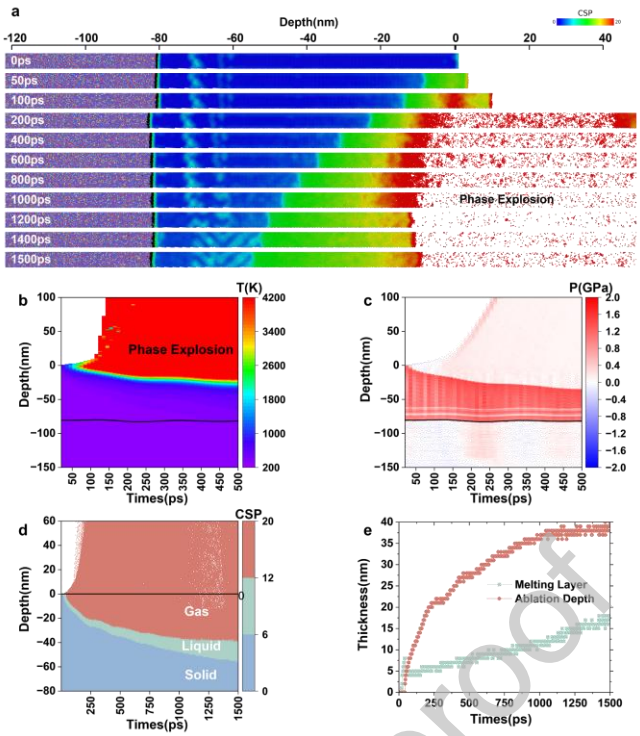

Fig. 4. TTM-MD simulation results of long-pulse laser irradiation on an 80 nm-thick Al film with a single 1 ns pulse and 27.5 J/cm^2 fluence. (a) Atomic snapshots. (b and c) Spatiotemporal distributions of (b) lattice temperature and (c) pressure. (d and e) Temporal evolution of (d) phase transition and (e) melting and ablation depth in Al.

The ns-pulse ablation was characterized by a thermally-dominated phase explosion mechanism. Within 50 ps, the metal surface temperature exceeds 1500 K, melting a 10 nm surface layer, as shown in Fig. 4(a). This was followed by phase explosion, where molten metal atoms rapidly disintegrated into vapor and small atomic clusters, ejecting from the surface. The ablation depth reached 37.5 nm by the end of the pulse, implying that two to three pulses would be required to remove the entire 80 nm film. Fig. 4(e) presents the temporal evolution of the ablation depth and molten layer thickness. The ablation rate progressively decreased with depth due to energy attenuation following the Beer-Lambert law. In contrast, the growth of the molten layer, governed by lattice thermal conduction, progressed steadily at a rate of 8.8 m/s and persisted even after the laser pulse ended.

Journal Pre-proof

Crucially, mechanical removal mechanisms were absent under ns-pulse irradiation. Although the ns pulse delivers higher pulse energy, its slow energy deposition accumulates minimal pressure and induces almost no tensile stress, as shown in Fig. 4(c). Notably, Fig. 4(a) reveals a phenomenon resembling spallation observed at 100 ps, characterized by the ejection of a ~10 nm surface layer. However, this was identified as a modeling defect arising from the misalignment between the fixed laser energy deposition zone and the rapidly expanding material surface. As shown in Fig. S6, this pseudo-spallation vanishes when the laser deposition surface is offset 10 nm above the material surface.

Interfacial stripping was also not observed since the prerequisite of sufficient epoxy deformation was not met. This deformation is necessary to provide the kinetic energy for metal ejection against the interfacial adhesion. However, the slow energy deposition failed to induce sufficient pressure, which was further relieved by the timely surface melting and phase explosion. Consequently, epoxy deformation remained below 3 nm throughout the entire ablation process.

While interfacial stripping is a characteristic mechanism of ultrafast lasers, it can occur in long-pulse laser ablation at substantially elevated fluences. The longer the pulse duration, the greater the laser fluence required for interfacial stripping to occur. When the pulse duration is 350 fs, only 0.17 J/cm^2 is needed (Fig. S3), whereas 11 J/cm^2 is required for 100 ps pulses (Fig. S7). Experimentally, He et al. [2] achieved the interfacial stripping of a primer on a metal substrate using a ns laser by simultaneously adjusting the laser power, scanning speed, and spacing to obtain an extremely high power density. Nevertheless, such high energy densities will considerably increase the risk of thermal damage. Therefore, short-pulse lasers offer a superior and non-compromising alternative for achieving clean interfacial stripping with minimal thermal impact.

Journal Pre-proof

3.2. Experimental verification through online high-speed imaging

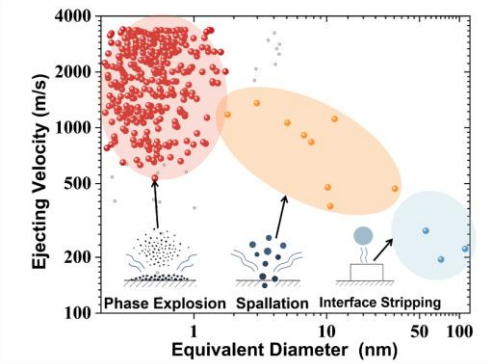

Fig. 5. Classification of material removal mechanisms based on atomic cluster analysis. The density plot of cluster velocity versus size reveals three distinct removal mechanisms: phase explosion, spallation, and interfacial stripping. Cluster size was given as the equivalent diameter (2 × radius of gyration).

Fig. 5 summarizes the metal cluster information obtained from the fs laser ablation simulation (covering Figs. 2 and S2–S5) and plots the relationship among cluster velocity, size, and quantity. Three laser ablation removal mechanisms are defined: spallation, phase explosion, and interfacial stripping. Phase explosion is typically observed in long-pulse laser ablation and high-fluence short-pulse laser processing. This thermally-dominated mechanism involves thermal melting and superheating, followed by the rapid ejection of dense nanoscale particle clusters, typically below 1 nm in size. In contrast, spallation is a thermomechanical mechanism that occurs when ultrafast-laser-induced tensile stress exceeds the material's yield strength, causing the fracture and ejection of larger material clusters of ~10 nm. Interfacial stripping, specific to layered materials, is also driven by tensile stress. However, a critical difference lies in the stress required to overcome the interfacial bonding strength, which is generally lower than the metal's intrinsic yield strength. This lower threshold facilitates the ejection of substantially larger clusters (up to micrometer-scale) at markedly slower velocities. For instance, as demonstrated in Fig. S8, interfacial stripping achieves a thickness of 1.47 μm. Notably, this

Journal Pre-proof

value reflected the limitations of the atomic model and available computational resources rather than the physical mechanism itself.

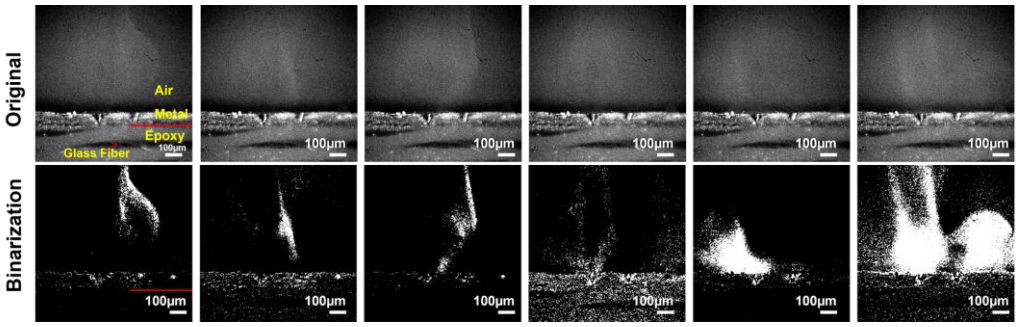

Fig. 6. High-speed imaging of the fs laser ablation plume during initial metal ablation (Stage 1). The homogeneous, fine smoke-like plume indicated the ejection of small clusters and vapor (e.g., phase explosion and spallation). The full dynamics are clearly shown in Movie S2.

To visualize the removal process, high-speed imaging was performed during fs laser scanning of a 73 μm-thick metal film on a GFRP substrate, as shown in Fig. 1(a). Fig. 6 shows a binarized snapshot of the early-stage ablation of pure metal (see Movie S2), where the laser focus is away from the epoxy interface. The removal was dominated by spallation and phase explosion. Materials were ejected primarily in the form of vapor or fine droplets, manifested as a rapidly diffusing, laser-scanning-modulated smoke-like plume at 35 × magnification, corresponding to the sub-50 nm clusters in Fig. 5.

As the ablation depth approached the metal/epoxy interface, interfacial stripping was initiated and became the dominant mechanism. As shown in Fig. 7(a), large molten droplets are visibly ejected from the groove at slower speeds (see Movie S3). Fig. 7(b) presents a comprehensive map of all ejected particles using long-exposure imaging techniques. The diameters of the observed ejected droplets were mainly distributed between 1 and 5 μm, with the largest reaching 7 μm. Moreover, during the interfacial stripping stage, the originally observed fine fumes almost completely disappeared, indicating that the spallation and phase explosion mechanisms were suppressed and that interfacial stripping became dominant. The

Journal Pre-proof

ejection velocity decreased with increasing droplet size, consistent with the trend in Fig. 5. Fig. 7(a) highlights the largest and slowest droplet, enabling precise observation of its complete trajectory. The slow ejection speed made it difficult for large droplets to escape, causing them to fall back onto the material surface. As shown in Fig. 7(c), metal particles 200 nm–5 μm in diameter are observed on the surface of the processed substrate. These particles were formed when molten liquid metal fell back and re-solidified, resulting in circular or elliptical shapes, which differed from the irregular rings and mesh-like features of the residual metal layer. These experimental observations strongly support the simulation results.

Therefore, the multi-pulse ablation process of micrometer-thick metal films was divided into two distinct stages. Initially, laser ablation removed the surface metal layer, where spallation and phase explosion acted as the dominant material removal mechanisms. During this stage, the laser-induced stress and thermal conduction were insufficient to penetrate the thick metal film and reach the substrate, preventing interfacial stripping. As the laser focus approached the interface, interfacial stripping initiated and became the dominant mechanism, while the contributions from the other two mechanisms were largely suppressed.

Journal Pre-proof

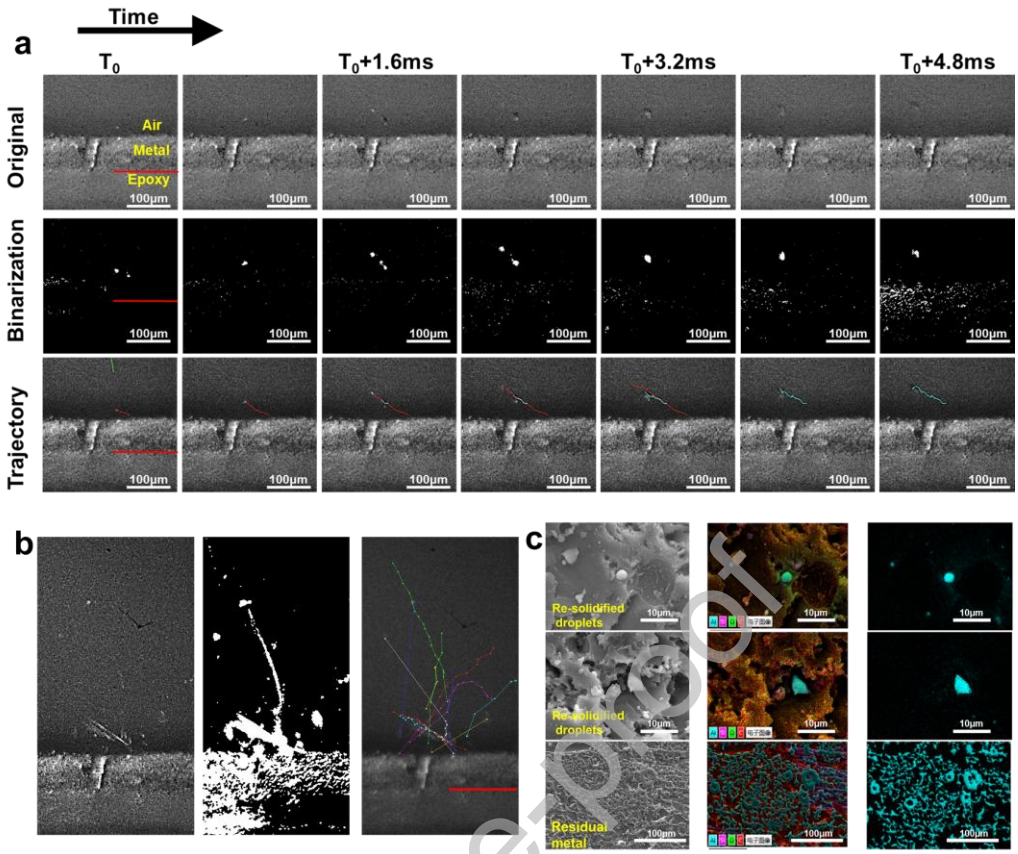

Fig. 7. Interfacial stripping and droplet fallback (Stage 2). (a) Time-resolved trajectory analysis of the large, slow-moving molten droplets induced by interfacial stripping. The full dynamics are demonstrated in Movie S3. (b) Long-exposure projection image. (c) Post-processed surface analysis showing two types of remnants: large, spherical droplets redeposited from the metal ejected during interfacial stripping and the network-like ablated remnant, as confirmed by SEM and EDS mapping.

Journal Pre-proof

3.3. The significance of interfacial stripping in practical processing

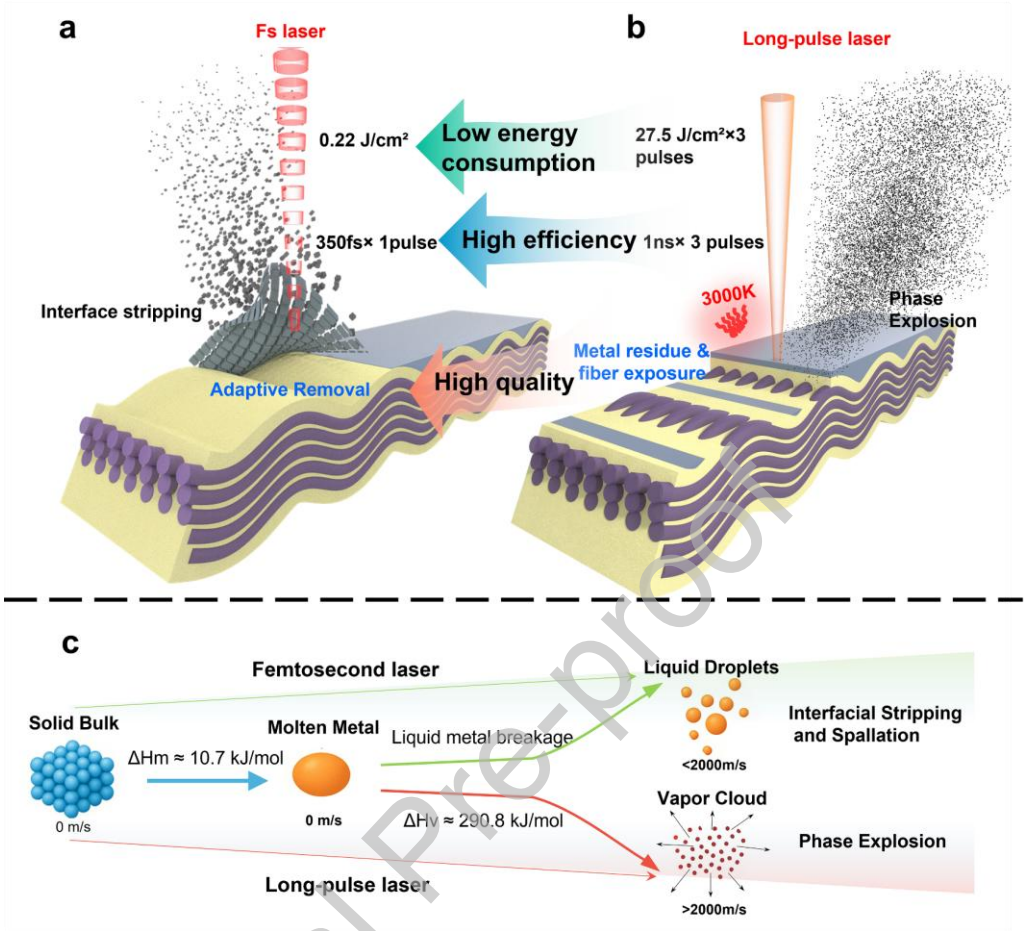

Fig. 8. Mechanisms and advantages of fs laser processing through interfacial stripping. (a and b) Schematic comparison of the processing effects: (a) fs laser and (b) long-pulse laser. (c) Energy consumption analysis.

The interfacial stripping mechanism, validated by both simulation and experiment, has demonstrated notable practical advantages for the fs laser processing of layered materials, particularly in substrate surface quality, processing uniformity, efficiency, and energy consumption.

Firstly, this mechanism minimizes thermal damage to the substrate. Complete removal of the thin film with minimal substrate damage presented a substantial challenge due to thermal effects. Epoxy resin is susceptible to pyrolysis above 573 K [66,67]. During interfacial stripping at 110 ps, the interfacial metal (CSP = 11) remained liquid, while the temperature of the adjacent

epoxy reached ~900 K, with a thermal penetration depth (> 573 K) of only about 5 nm. In contrast, long-pulse ablation via phase explosion exposed the material to temperatures exceeding 3000 K. Crucially, interfacial stripping occurred rapidly, before the interfacial metal underwent extensive vaporization or reached its peak temperature.

Secondly, interfacial stripping enables thickness-adaptive processing, thereby improving the machining uniformity. In practical applications, thin films often exhibit nonuniform thickness due to uneven deposition or substrate periodic structures. For example, the woven glass fiber in our substrate created a periodic surface, leading to a correspondingly varying metal thickness (Fig. S1). Long-pulse laser ablation, with its strictly linear energy-removal relationship, inevitably causes defects, even under optimized parameters. Excessive energy damages the substrate, while insufficient energy leaves residual film, as shown in Fig. 8(b). In contrast, fs-laser-induced interfacial stripping is nonlinear and threshold-dependent for a given film thickness. This implies that a specific fluence can induce stripping across a range of film thicknesses. For example, in Figs. 2 and S2, a fluence of 0.22 J/cm^2 achieves simultaneous removal of metal layers ranging from 80 to 150 nm. This inherent adaptability allows laser parameters to compensate for thickness variations, significantly improving processing uniformity, as shown in Fig. 8(a).

Thirdly, fs laser processing offers superior efficiency and reduced energy consumption. An 80 nm Al film was completely ablated with a single fs-laser pulse at a fluence of only 0.17 J/cm^2, whereas ns-laser ablation required 55–82.5 J/cm^2 (two to three pulses at 27.5 J/cm^2). The significant disparity (over 300 times) stems from the fundamental energy requirements of the underlying mechanisms, as shown in Fig. 8(c). Long-pulse laser ablation, dominated by phase explosion, required overcoming the substantial enthalpy of vaporization ($\Delta H_v \approx 290.8$ kJ/mol for Al [68,69]) to fully disintegrate metal into monatomic vapor. In contrast, fs-laser-induced spallation and interfacial stripping proceeded through mechanical fracturing of molten metal,

requiring only melting enthalpy ($\Delta H_m \approx 10.7$ kJ/mol) to liquefy the metal and fracture energy to overcome liquid cohesion or interfacial adhesion. Furthermore, the violent vapor and small atomic clusters produced by explosions typically have extremely high ejection velocities (Fig. 5), implying significant metal superheating as the source of kinetic energy. Therefore, most of the long-pulse laser energy is wasted on the vaporization enthalpy change of metal from liquid to gas (~27 times that of the melting enthalpy) and the excessive kinetic energy of atomic clusters, which are both unnecessary for thin film removal. The thermomechanical mechanism neatly achieves a more energy-efficient material removal strategy by avoiding complete vaporization.

3.4. fs laser experiment

3.4.1. Optimization of laser processing parameters

Laser parameters directly determine the quality and outcomes of the process. Among numerous parameters, laser power and scanning speed have been identified as the most critical factors [12,70]. Accordingly, a systematic single-factor experimental design was employed to investigate their effects. Laser power was selected at five equally spaced levels within the range of 0.8–10.5 W, covering the transition from threshold ablation to severe over-ablation. Scanning speed was selected at five equally spaced levels within the range of 100–900 mm/s. This range could effectively characterize varying processing efficiencies and thermal accumulation effects. Other variables were kept constant, including pulse repetition frequency (100 kHz), scan line spacing (15 μm), scanning strategy (bidirectional, single pass in each direction), defocus amount (0, surface focus), and laser spot diameter (20 μm). The energy density was obtained by calculating the total laser energy delivered per unit area, as described in the Supplementary Materials [12].

Journal Pre-proof

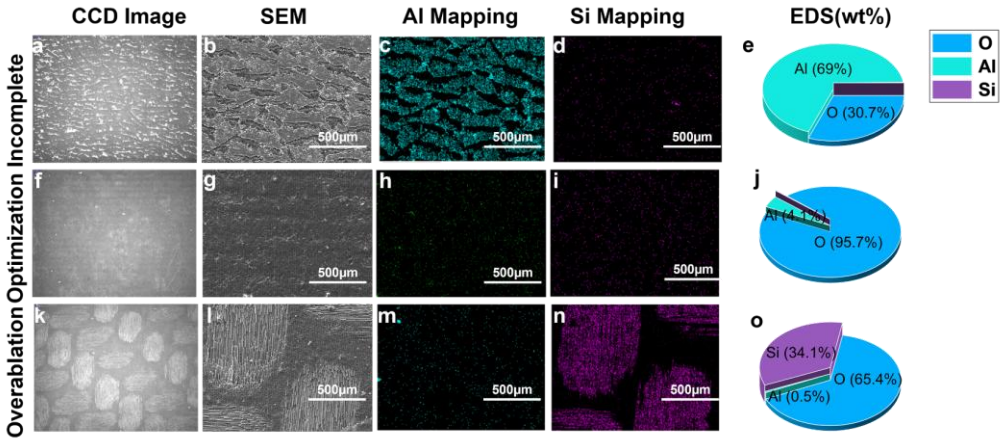

Fig. 9. Optimization of laser processing parameters. This figure compares three processing regimes at a fixed laser power (5.1 W) and varying scanning speeds: (a–e) residual metal at a high speed (900 mm/s, 11.33 J/cm^2), (f–j) optimal ablation at an intermediate speed (700 mm/s, 14.6 J/cm^2), and (k–o) substrate overablation at a low speed (500 mm/s, 20.4 J/cm^2). Characterization was conducted using a charge-coupled device camera, SEM (80 ×), and EDS mapping/quantification.

As expected, lower scanning speeds and higher laser powers resulted in more severe ablation. Fig. 9 presents a comparative analysis of three characteristic processing regimes: incomplete ablation (5.1 W, 900 mm/s, 11.33 J/cm^2), optimal processing (5.1 W, 700 mm/s, 14.6 J/cm^2), and overablation (5.1 W, 500 mm/s, 20.4 J/cm^2). At 900 mm/s, the low spot overlap rate results in incomplete metal removal. Due to the higher reflectivity (Fig. S9), the metal appears overexposed under illumination, as shown in Fig. 9(a). In the EDS elemental maps, cyan-colored regions indicate residual Al metal, suggesting incomplete metal removal. Purple-colored regions correspond to the exposure of the underlying glass fiber (SiO_2) substrate, implying damage to the epoxy layer. At 700 mm/s, an optimally processed surface is achieved, as shown in Fig. 9(f and g). The resulting Ra is 1.8 μm, comparable with the original substrate Ra of 1.6 μm. Critically, the EDS result shown in Fig. 9(h–j) confirms that Al and Si are almost absent. The carbon-to-oxygen elemental ratio of 4.94 closely matches that of the pristine epoxy

Journal Pre-proof

substrate (4.64), suggesting minimal thermal degradation and negligible oxidation. Further reducing the scanning speed to 500 mm/s results in overablation, damage to the epoxy layer, and exposure of the underlying glass fibers, some of which exhibited signs of fracture, as shown in Fig. 9(k and l). A significant amount of silicon is detected in Fig. 9(n and o). Based on a comprehensive analysis of surface morphology and EDS results, the optimal processing parameters were identified as a scanning speed of 700 mm/s and a laser power of 5.1 W, corresponding to an energy density of 14.6 J/cm^2.

3.4.2. Thermochemical damage of the substrate

To analyze the damage mechanism of the substrate, FTIR and XPS were used to investigate the changes in functional groups in the epoxy following laser scanning. Based on prior pyrolysis and photolytic studies [71–74], as well as bond dissociation energies (Fig. 10(a) inset) [75], the degradation pathway of Diglycidyl ether of bisphenol A (DGEBA) epoxy was found to initiate with the cleavage of C-C bonds in the isopropyl group, followed by their oxidation to C-O. The subsequent breakdown of the backbone C-C and aromatic ether (C-O-C) linkages unraveled the polymer chain, ultimately leading to the further oxidation of C-O bonds into C=O bonds and the formation of compounds like phenyl formates.

As shown in Fig. 10(a), FTIR results reveal that the main characteristic peaks (e.g., aromatic ether at ~1050 cm^{-1} and aromatic rings at 1538/1480 cm^{-1}) do not grow or disappear after scanning but only weaken in intensity, indicating that the overall chemical composition is retained. However, a slight attenuation of peaks associated with the isopropyl group (1183 cm^{-1}) and the stretching vibration of the aromatic ether (1050 cm^{-1}) indicates initial oxidative damage (C-O) and subtle chain scission. Critically, no emergent peaks are detected in the carbonyl region (1900–1500 cm^{-1}), confirming that oxidation halts at the C-O stage without progressing to C=O. This suggests a remarkably low degree of fs-laser-induced oxidation.

In parallel, XPS surface analysis corroborated and quantified this oxidative damage. Survey scans revealed substantial chemical alterations: a 15% increase in oxygen content, the presence of 6% residual aluminum, and a 22% decrease in carbon content. High-resolution C 1*s* fitting results shown in Fig. 10(b and c) demonstrate that ~30% of carbon bonds are converted from C-C/C-H (284.8 eV) to C-O (286.4 eV). The consistent intensity of the C=O component (288.6 eV) before and after processing affirms that oxidation is primarily confined to the preliminary conversion of aliphatic carbons, with minimal formation of highly oxidized species.

Whereas FTIR and EDS (both with micron-scale sampling depths [76,77]) detected no bulk chemical degradation, XPS (2–10 nm sampling depth [76,77]) identified pronounced localized oxidation. This stark contrast conclusively established that thermochemical damage is confined to the nanoscale surface region, preserving the integrity of the bulk material beneath.

The degradation of mechanical properties across different length scales was characterized using nanoindentation and Vickers microhardness testing, as shown in Figs. 10(d) and S10. Under quasistatic loading to a maximum load of 2 mN, which results in indentation depths of approximately 400 and 700 nm, respectively, the irradiated substrate exhibits significant tensile residual stress, likely attributable to thermal expansion and interfacial stripping. A substantial degradation in nanomechanical properties is observed, with reductions of 68% in nanohardness and 40% in elastic modulus. The load-displacement curves further indicate enhanced creep compliance. Collectively, these results confirmed significant mechanical degradation within the nanoscale surface region. However, the superior mechanical performance of GFRP in practical applications is governed by its composite structure, where high-strength glass fibers serve as the principal load-bearing component [78]. In a GFRP substrate approximately 1 mm thick, the degradation of mechanical properties in the surface layer (representing less than 0.1% of the total thickness) had a negligible impact on macroscopic performance. This was demonstrated

by the Vickers hardness measurements (Fig. S10), which show only a 7.5% decrease after laser processing, a level of damage considered acceptable for practical applications.

Finally, patterned arrays fabricated under optimal parameters achieve 350 μm features with 64 μm line widths, as shown in Fig. 10(e), validating the high-precision fs laser processing capability. Collectively, these multifaceted analyses demonstrated that fs laser etching enabled micron-scale patterning of metal films on epoxy substrates while restricting thermal damage to a superficial nanoscale layer, thereby fulfilling the stringent requirements for advanced electronic and functional microstructure applications.

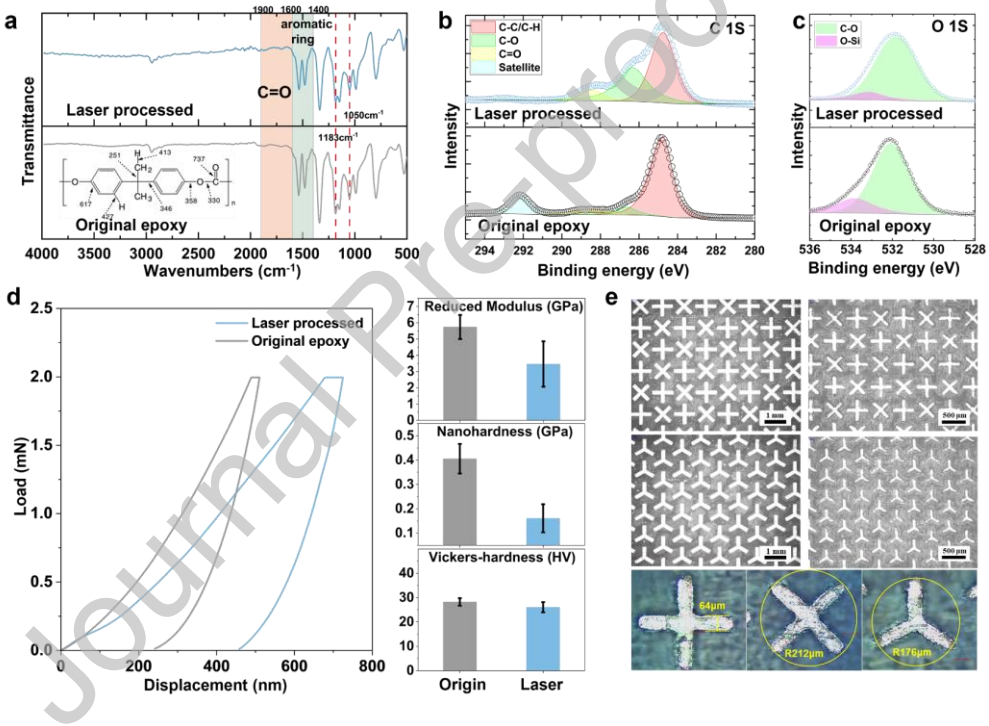

Fig. 10. Comprehensive analysis of the subsurface damage of the epoxy substrate by fs laser processing. (a) FTIR spectra of the original and laser-processed epoxy. Key vibrational modes are labeled. The inset (reproduced from [72]) shows the bond dissociation energies of the DGEBA model compound, illustrating the predicted thermo-oxidative degradation pathway. (b and c) High-resolution XPS spectra of (b) C 1*s* and (c) O 1*s* regions. (d) Evolution of the mechanical properties of the substrate epoxy, including nanoindentation load-displacement curves, reduced modulus, nanohardness, and Vickers-hardness. (e) Optical micrograph of a

representative functional microstructure fabricated under optimal parameters, demonstrating that nanoscale damage does not compromise micron-scale functional precision.

4. Conclusions

In summary, this study elucidates the thermomechanical removal mechanisms and thermochemical substrate damage mechanisms involved in fs laser processing of Al/GFRP layered materials. By extending the TTM-MD model to layered interfaces, we reveal the complete process and conditions for a unique removal mechanism—interfacial stripping—which is further validated by high-speed imaging. Three distinct removal mechanisms (phase explosion, spallation, and interfacial stripping) are identified through a statistical atomic cluster analysis. Our findings provide atomistic insights into the advantages of low energy consumption, high efficiency, and superior processing quality afforded by ultrafast laser ablation. Experimentally, the aluminum layer was completely removed using optimized laser parameters. Multimethod characterization using EDS, XPS, and FTIR confirms that thermal oxidation and substrate damage are limited to a nanoscale-affected layer. Finally, evaluations of surface roughness, mechanical properties, and microfabrication precision collectively attest to the practicality and versatility of the process.

Acknowledgements

The research is funded by the National Natural Science Foundation of China (Nos. 52475473 and 20221017-16), the Jinan Science and Technology Bureau (No. 202333034), and the Shandong Province Key Research and Development Plan (No. 2024JMRH0308). The authors also acknowledge the support of the Scientific Research Innovation Team of Young Scholars in Colleges and Universities of Shandong Province (No. 2020KJB001) and the Shandong Key Laboratory of High Performance Tools and System.

Journal Pre-proof

References

[1] G. Yang, Y. Liu, L. Liu, W. Xiong, L. Deng, S. Zhao, J. Manuf. Process. 135 (2025) 230–239.

[2] Z. He, S. Zheng, Y. Shen, J. Tao, W. Xiong, S. Shu, X. Zeng, S. Song, J. Mater. Sci. Technol. 190 (2024) 10–23.

[3] Y. Konishi, J. Yan, Nanomanuf. Metrol. 8 (2025) 6.

[4] Q. Yang, Z. Hu, M.H. Seo, Y. Xu, Y. Yan, Y.H. Hsu, J. Berkovich, K. Lee, T.L. Liu, S. McDonald, H. Nie, H. Oh, M. Wu, J.T. Kim, S.A. Miller, Y. Jia, S. Butun, W. Bai, H. Guo, J. Choi, A. Banks, W.Z. Ray, Y. Kozorovitskiy, M.L. Becker, M.A. Pet, M.R. MacEwan, J.K. Chang, H. Wang, Y. Huang, J.A. Rogers, Nat. Commun. 13 (2022) 6518.

[5] G. Yang, Y. Ding, L. Liu, H. Yang, X. Wu, W. Xiong, L. Deng, J. Mater. Process. Technol. 312 (2023) 117868.

[6] Y. Feng, H. Yang, H. Shen, J. Zhou, Precis. Eng. 89 (2024) 430–437.

[7] G.W. Huang, Q.P. Feng, H.M. Xiao, N. Li, S.Y. Fu, ACS Nano 10 (2016) 8895–8903.

[8] F. Zacharatos, M. Makrygianni, R. Geremia, E. Biver, D. Karnakis, S. Leyder, D. Puerto, P. Delaporte, I. Zergioti, Appl. Surf. Sci. 374 (2016) 117–123.

[9] G.X. Zhou, Z. Zhao, Y. Zhang, W. Liu, Z.H. Yang, D.C. Jia, Y. Zhou, J. Mater. Sci. Technol. 111 (2022) 49–56.

[10] S. Zeng, Y. Liu, S. Li, K. Shen, Z. Hou, A.P. Chooi, A.T. Smith, Z. Chen, L. Sun, Adv. Funct. Mater. 31 (2021) 2009481.

[11] S. Wang, T. Li, T. Liu, G. Wang, L. Wang, L. Dong, Y. Wang, F. Zuo, M. Sun, J. Guo, C. Li, H. Xu, Z. Wang, Z. Weng, Nanomanuf. Metrol. 8 (2025) 3.

[12] Z. Huang, Y. Cai, F. Xue, Y. Han, Q. Song, B. Wang, Z. Liu, Appl. Surf. Sci. 638 (2023) 158113.

[13] A. Alwaidh, M. Sharp, P. French, Opt. Lasers Eng. 58 (2014) 109–113.

Journal Pre-proof

[14] L. Gao, Q. Zhang, M. Gu, Int. J. Extreme Manuf. 7 (2025) 022010.

[15] J. Huang, K. Xu, S. Xu, Int. J. Mach. Tools Manuf. 205 (2025) 104246.

[16] X. Jia, J. Luo, K. Li, C. Wang, Z. Li, M. Wang, Z. Jiang, V.P. Veiko, J. Duan, Int. J. Extreme Manuf. 7 (2025) 032001.

[17] S. Zhou, K. Zhao, H. Shen, Opt. Laser Technol. 132 (2020) 106495.

[18] F. Matsumoto, M. Yamada, M. Tsuta, S. Nakamura, N. Ando, N. Soma, Int. J. Extreme Manuf. 5 (2022) 012001.

[19] P. Zhu, A. Boyce, S.R. Daemi, B. Dong, Y. Chen, S. Guan, M. Crozier, Y.L. Chiu, A.J. Davenport, R. Jervis, P. Shearing, R.N. Esfahani, P.R. Slater, E. Kendrick, Energy Storage Mater. 69 (2024) 103373.

[20] Y. Hu, H. Wang, D. Wang, X. Xia, N. Liu, T. Yang, B. Li, C. Liang, J. Mater. Sci. Technol. 206 (2025) 88–99.

[21] G. He, J. Li, H. Han, J. Yan, J. Xie, M. Luo, Y. Zhao, Y. Cheng, M. Qiao, J. Mater. Process. Technol. 341 (2025) 118902.

[22] B. Wang, P. Wang, J. Song, Y.C. Lam, H. Song, Y. Wang, S. Liu, J. Mater. Process. Technol. 308 (2022) 117716.

[23] V.E. Alexopoulou, A.P. Markopoulos, Arch. Comput. Methods Eng. 31 (2024) 93–123.

[24] S.I. Anisimov, B.L. Kapeliovich, T.L. Perelman, Zh. Eksp. Teor. Fiz. 66 (1974) 776–781.

[25] H. Liu, W. Xie, Y. Ding, K. Chen, S. Wang, H. Huo, L. Yang, Nanoscale 16 (2024) 21189–21215.

[26] S. Song, Q. Lu, P. Zhang, H. Yan, H. Shi, Z. Yu, T. Sun, Z. Luo, Y. Tian, Opt. Laser Technol. 159 (2023) 109001.

[27] D.S. Ivanov, L.V. Zhigilei, Phys. Rev. B 68 (2003) 064114.

[28] J. Guo, P. Ji, L. Jiang, G. Lin, Y. Meng, Powder Technol. 407 (2022) 117682.

[29] Y. Zhou, D. Wu, G. Luo, Y. Hu, Y. Qin, J. Manuf. Process. 77 (2022) 783–793.

Journal Pre-proof

[30] G. Lin, L. Jiang, P. Ji, J. Sun, J. Hu, Y. Lian, Opt. Laser Technol. 180 (2025) 111404.

[31] J. Xie, J. Yan, D. Zhu, G. He, Adv. Funct. Mater. 32 (2022) 2108802.

[32] A. Amouye Foumani, D.J. Förster, H. Ghorbanfekr, R. Weber, T. Graf, A.R. Niknam, Appl. Surf. Sci. 537 (2021) 147775.

[33] Q. Xiong, Z. Li, T. Kitamura, Sci. Rep. 7 (2017) 9218.

[34] Y. Ihm, D.H. Cho, D. Sung, D. Nam, C. Jung, T. Sato, S. Kim, J. Park, S. Kim, M. Gallagher-Jones, Y. Kim, R. Xu, S. Owada, J.H. Shim, K. Tono, M. Yabashi, T. Ishikawa, J. Miao, D.Y. Noh, C. Song, Nat. Commun. 10 (2019) 2411.

[35] M.I. Arefev, M.V. Shugaev, L.V. Zhigilei, Sci. Adv. 8 (2022) eabo2621.

[36] S. Zhou, H. Shen, J. Manuf. Process. 84 (2022) 469–480.

[37] Z. Zhang, Z. Yang, C. Wang, Q. Zhang, S. Zheng, W. Xu, Opt. Laser Technol. 133 (2021) 469–480.

[38] G. Lin, L. Jiang, J. Hu, Z. Chen, Z. Ning, W. Han, J. Mater. Sci. Technol. 252 (2025) 190–205.

[39] D. Yang, Z. He, M. Zhang, Y. Liu, L. Li, J. Manuf. Process. 131 (2024) 984–1000.

[40] Y. Lian, J. Sun, Z. Zhang, G. Lin, Z. Chen, Y. Yuan, Surf. Coat. Technol. 483 (2024) 130756.

[41] J. Liu, M. Wu, Z. Sun, Q. Zhang, Y. Zhu, Y. Fu, Appl. Surf. Sci. 661 (2024) 160022.

[42] J. Zhao, X. Han, F. Dong, S. Liu, J. Manuf. Process. 137 (2025) 252–262.

[43] X. He, R. Chen, J. Xie, Opt. Laser Technol. 190 (2025) 113171.

[44] L.V. Zhigilei, Z. Lin, D.S. Ivanov, J. Phys. Chem. C 113 (2009) 11892–11906.

[45] Y. Lian, L. Jiang, J. Sun, W. Tao, Z. Chen, G. Lin, Z. Ning, M. Ye, Nanophotonics 12 (2023) 4461–4473.

[46] Y. Lian, M. Liang, R. You, J. Mater. Res. Technol. 37 (2025) 1784–1797.

[47] A.K.M.S. Ali, I. Ahmed, Mater. Res. Express 8 (2021) 065201.

Journal Pre-proof

[48] J. Schindelin, I. Arganda-Carreras, E. Frise, V. Kaynig, M. Longair, T. Pietzsch, S. Preibisch, C. Rueden, S. Saalfeld, B. Schmid, J.Y. Tinevez, D.J. White, V. Hartenstein, K. Eliceiri, P. Tomancak, A. Cardona, Nat. Methods 9 (2012) 676–682.

[49] S.I. Anisimov, B.S. Luk'yanchuk, Phys. Usp. 45 (2002) 293.

[50] D.M. Duffy, A.M. Rutherford, J. Phys.-Condens. Matter 19 (2006) 016207.

[51] A.M. Rutherford, D.M. Duffy, J. Phys.-Condens. Matter 19 (2007) 496201.

[52] A.P. Thompson, H.M. Aktulga, R. Berger, D.S. Bolintineanu, W.M. Brown, P.S. Crozier, P.J. in 't Veld, A. Kohlmeyer, S.G. Moore, T.D. Nguyen, R. Shan, M.J. Stevens, J. Tranchida, C. Trott, S.J. Plimpton, Comput. Phys. Commun. 271 (2022) 108171.

[53] P. Dauber-Osguthorpe, V.A. Roberts, D.J. Osguthorpe, J. Wolff, M. Genest, A.T. Hagler, Proteins 4 (1988) 31–47.

[54] V.V. Zhakhovskii, N.A. Inogamov, Yu.V. Petrov, S.I. Ashitkov, K. Nishihara, Appl. Surf. Sci. 255 (2009) 9592–9596.

[55] H. Heinz, R.A. Vaia, B.L. Farmer, R.R. Naik, J. Phys. Chem. C 112 (2008) 17281–17290.

[56] C. Schäfer, H.M. Urbassek, L.V. Zhigilei, B.J. Garrison, Comput. Mater. Sci. 24 (2002) 421–429.

[57] D. Iabbaden, J. Amodeo, C. Fusco, F. Garrelie, J.P. Colombier, Phys. Rev. Mater. 6 (2022) 126001.

[58] J. Xu, D. Xue, O. Gaidai, Y. Wang, S. Xu, Processes 11 (2023) 1704.

[59] F. Ye, Y. Chen, L. Cai, Y. Lu, Y. Ye, Y. Ren, Chin. J. Lasers 51 (2024) 1602408.

[60] C.L. Kelchner, S.J. Plimpton, J.C. Hamilton, Phys. Rev. B 58 (1998) 11085–11088.

[61] H. Conrad, JOM 16 (1964) 582–588.

[62] A.E. Mayer, P.N. Mayer, Int. J. Mech. Sci. 157–158 (2019) 816–832.

[63] Q.Y. Liu, J. Zhou, Y.W. Zhao, L.C. Xiong, T.L. Shi, Y.H. Long, Comput. Mater. Sci. 160 (2019) 420–429.

Journal Pre-proof

[64] B. Tian, W. Ma, S. Chen, F. Sun, X. Wang, Int. J. Refract. Met. Hard Mater. 119 (2024) 106560.

[65] H. An, J. Wang, F. Fang, Opt. Laser Technol. 158 (2023) 108863.

[66] C. Ma, D. Sánchez-Rodríguez, T. Kamo, J. Hazard. Mater. 412 (2021) 125329.

[67] M. Xu, J. Di, Y. Wu, X. Meng, H.W. Ji, H. Jiang, J. Li, Q. Lu, Chem. Eng. J. 473 (2023) 145404.

[68] J. Howe, Interfaces in Materials: Atomic Structure, Thermodynamics and Kinetics of Solid-Vapor, Solid-Liquid and Solid-Solid Interfaces, John Wiley & Sons, Inc., 1997.

[69] D.A. Porter, K.E. Easterling, M.Y. Sherif, Phase Transformations in Metals and Alloys, 4th ed., CRC Press, Boca Raton, 2021.

[70] C. Zheng, Y. Cai, P. Zhang, T. Zhang, J. Aslam, Q. Song, Z. Liu, J. Manuf. Process. 119 (2024) 57–65.

[71] B. Mailhot, S. Morlat-Thérias, M. Ouahioune, J.-L. Gardette, Macromol. Chem. Phys. 206 (2005) 575–584.

[72] B.N. Jang, C.A. Wilkie, Thermochim. Acta 426 (2005) 73–84.

[73] M. Celiński, M. Sankowska, J. Loss Prev. Process Ind. 44 (2016) 125–131.

[74] S. Zhao, C. Chen, M. Haga, M. Ueshima, H. Hirahara, J. Sang, S.H. Cho, T. Sekino, K. Suganuma, Compos. Pt. B-Eng. 254 (2023) 110562.

[75] K.B. Abbås, Polymer 21 (1980) 936–940.

[76] A.S. Gorzalski, C. Donley, O. Coronell, J. Membr. Sci. 522 (2017) 31–44.

[77] P. Luan, G.S. Oehrlein, Langmuir 35 (2019) 4270–4277.

[78] Z. Wang, Y. Ma, B. Yuan, C. Wu, C. Li, S. Sun, Sensors 23 (2023) 3659.

Journal Pre-proof

Graphical abstract

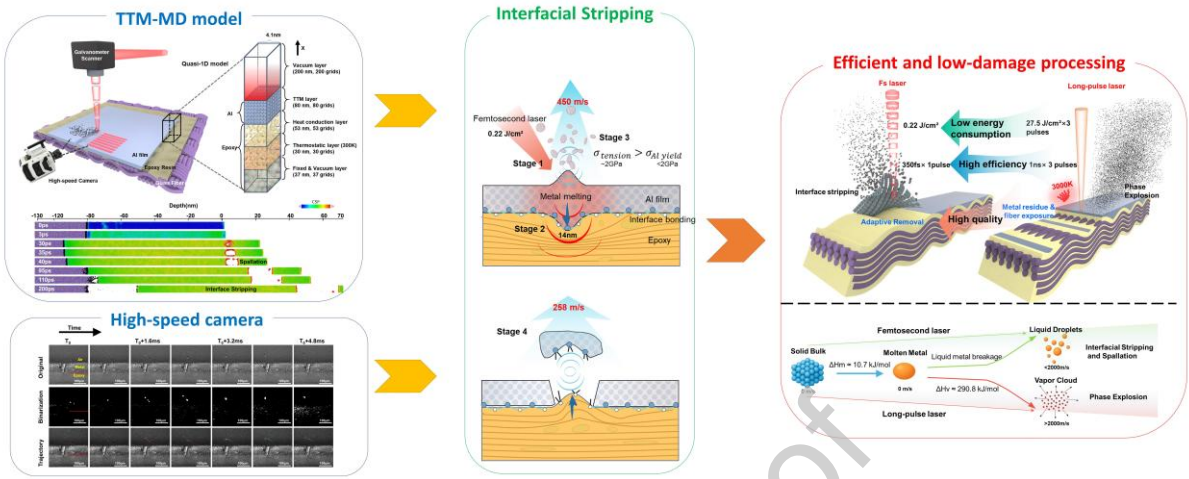

Declaration of Interest Statement

☒ The authors declare that they have no known competing financial interests or personal relationships that could have appeared to influence the work reported in this paper.

Journal Pre-proof